applied sciences

MDPI

Article

System and Method for Reducing NLOS Errors in UWB Indoor Positioning

Yifan Wang [1,2], Di Zhang [3,*], Zengke Li [2,4], Ming Lu [3], Yunfei Zheng [3] and Tianye Fang [3]

[1] Joint Laboratory of Power Remote Sensing Technology, Electric Power Research Institute, Yunnan Power Grid Co., Ltd., Kunming 650217, China; wangyifan@yn.csg.cn
[2] School of Environment and Spatial Informatics, China University of Mining and Technology, Xuzhou 221116, China; zengkeli@cumt.edu.cn
[3] School of Geodesy and Geomatics, Wuhan University, Wuhan 430079, China; luming@whu.edu.cn (M.L.); zhengyunfei@whu.edu.cn (Y.Z.); tianyefang@whu.edu.cn (T.F.)
[4] Key Laboratory of Resource and Environmental Information Engineering, China University of Mining and Technology, Xuzhou 221116, China
* Correspondence: dzhang@sgg.whu.edu.cn

Abstract: The ultra-wideband (UWB) technology has been increasingly recognized as an efficacious strategy for Indoor Positioning Systems (IPSs). However, the accuracy of the UWB system can be severely degraded by non-line-of-sight (NLOS) errors. In this study, we proposed a new method to reduce the UWB positioning error in such an indoor environment. We developed a system consisting of a Robotic Total Station (RTS), four UWB base stations, a moving target (including a prism and a UWB tag), and a PC. The observed coordinates of the moving target, captured using millimeter precision from an RTS device, served as the ground truth for calculating the positioning errors of the UWB tag. In a significant NLOS scenario, the UWB's three-dimensional positioning error was identified to exceed the nominal value declared by the manufacturer by a factor of more than three. A detailed analysis revealed that each coordinate component's error distribution pattern demonstrated considerable variance. To reduce the NLOS error, we designed a combined multilayer neural network that simultaneously fits errors on all three coordinate components and three separate multilayer networks, each dedicated to optimizing errors on a single coordinate component. All networks were trained and verified by benchmark errors obtained from the RTS. The results showed that neural networks outperform the traditional methods, attributed to their strong nonlinear modelling ability, thereby significantly improving the external accuracy by an average reduction in RMSE by 61% and 72%. It is evident that the proposed separate networks would be more suitable for NLOS positioning problems than a combined network.

Keywords: ultra-wideband; robotic total station; neural network; indoor positioning

Citation: Wang, Y.; Zhang, D.; Li, Z.; Lu, M.; Zheng, Y.; Fang, T. System and Method for Reducing NLOS Errors in UWB Indoor Positioning. *Appl. Sci.* **2024**, *14*, 5123. https://doi.org/10.3390/app14125123

Received: 14 May 2024
Revised: 4 June 2024
Accepted: 8 June 2024
Published: 12 June 2024

1. Introduction

Indoor Positioning Systems (IPSs) are crucial in diverse fields, from emergency services to industrial automation [1]. The most used satellite technologies, like the Global Navigation Satellite System (GNSS) [2], are ineffective indoors due to signal attenuation caused by building materials and environmental factors [3]. Ultra-wideband (UWB) technology has been increasingly recognized as an efficacious strategy for IPSs due to its high accuracy, low transmission cost, and robustness to environmental perturbations [4]. The Federal Communication Commission (FCC) defines the UWB signal by one of the two conditions: (1) The signal bandwidth should be wider than 0.2 times the carrier frequency, or (2) the signal bandwidth should be wider than 500 MHz. The fine time resolution and broad bandwidth of UWB technology enable precise location tracking, making it superior to other IPSs like WiFi or Bluetooth [5], especially in complex indoor scenarios. For instance, Ridolfi et al. demonstrated UWB's capability to track athletes with an average

error of 20 cm [6]. Similarly, Cheng et al. showcased the precision of UWB in static and dynamic item tracking within an indoor environment [7]. Park et al. introduced a system integrating BIM with UWB for accurate indoor navigation and robot tracking, enhancing construction efficiency and safety [8]. Wang, et al. [9] proposed a trust-assessment-based distributed localization algorithm that can achieve accurate localization.

However, the accuracy of the UWB system is affected by various error sources. Notably, non-line-of-sight (NLOS) conditions can degrade positioning accuracy substantially due to signal obstruction, with errors up to several meters [10,11]. Multipath propagation, due to NLOS signals in combination with the original LOS signal [12], introduces errors ranging from a few centimeters to over a meter [13], depending on environmental complexity [14]. Multipath error is more common but much easier to ignore, more difficult to avoid, and significantly impacts positioning accuracy. Additionally, synchronization errors between devices and clock drift can also contribute to inaccuracies, typically within tens of centimeters [15].

Several correction methods have been developed to mitigate these challenges. Kalman-filter-based algorithms are commonly used to minimize ranging errors [16,17]. The twice correction algorithm, combining linear fitting and polynomial methods, enhances both static and dynamic positioning accuracy [18]. Multi-sensor data fusion techniques, such as integrating UWB with inertial measurement units (IMUs) and encoders, employ Kalman filtering to enhance positioning accuracy by leveraging the complementary strengths of different sensors [19]. Despite improvements, the complexity of sensor integration [20] and the need for extensive calibration [21] can limit these methods. NLOS identification and mitigation strategies aim to detect and correct the additional path length caused by obstacles [22], but they often require complex environmental modeling [23].

The development of neural networks has introduced new possibilities for error correction in UWB indoor positioning. Neural networks can learn complex patterns and relationships from data [24], which implies their capability to correct the nonlinear error characteristics in complicated environments. The neural network can be integrated into UWB-based algorithms and maintain a stable accuracy in NLOS scenarios [25]. Another study by Leyla Nosrati et al. utilized deep learning algorithms, including multilayer perceptron (MLP) and convolutional neural networks (CNNs), to reduce ranging errors caused by multipath components [26]. However, one possible side effect of a complex network structure is that it always needs a large amount of data and a long training time, which also brings inconvenience to use. Furthermore, retrieving more accurate and reliable reference values for training neural networks is still a challenging issue for researchers.

Robotic Total Stations (RTSs) have gained significant attention for their versatile applications in various fields, especially in environments where the GNSS signal is unreliable [27]. In outdoor environments, RTSs are the preferred choice to obtain high-accuracy measurements in the order of millimeters. In indoor robot navigation, their contribution is marked by high precision and stability [28]. However, few studies use RTS to correct UWB locations.

Therefore, this paper presents the following main contributions:

(1) A method for improving the UWB positioning accuracy is proposed. Synchronous RTS coordinate observations at the mm level are used as the benchmark value for the UWB positioning error, which are then inputted into the neural network for training.
(2) An experimental system for data acquisition was designed and developed, including control software running on a PC, one RTS, four UWB base stations, and a moving target consisting of a prism and a UWB tag.
(3) Two kinds of neural networks (a combined neural network that fits all three coordinate components concurrently and three separate networks dedicated to optimizing a single coordinate component) and two traditional methods (a polynomial model and a locally weighted linear regression model) were compared. An evaluation was implemented using external coincidence accuracy based on the result from the verification dataset.

The remainder of this paper is organized as follows: Section 2 introduces the basic idea and steps of our method, including a description of the UWB and RTS experimental sets in Sections 2.1 and 2.2, respectively; an introduction of the control software is in Section 2.3, and Section 2.4 describes the matching method for the RTS and UWB observations. Experimental steps are listed in Section 3.1, the neural network structure is given in Section 3.2, two traditional techniques are provided in Section 3.3, and Section 3.4 shows the accuracy indicators for the network evaluation. Section 4 presents the results and discussion of the validation and testing experiments. Finally, our conclusions are drawn in Section 5.

2. Materials and Methods

2.1. The Ultra-Wideband

The D-DWM-PG1.7 UWB board, as illustrated in Figure 1, is produced by Lenet Technology Co., Ltd., situated in Guangzhou, China. This board is developed utilizing the DW1000 positioning chip, a product of Decawave Ltd., which is headquartered in Dublin, Ireland.. Its main technical specification is listed in Table 1. The distance between a pair of such modules can be ascertained with an accuracy of ±10 cm by measuring signal propagation time. This is achieved by employing two-way ranging utilizing time-of-flight (TOF) or one-way ranging using the time difference of arrival (TDOA) method. Based on the principle of distance intersection, the three-dimensional coordinates of a tag can be determined with an accuracy of ±30 cm.

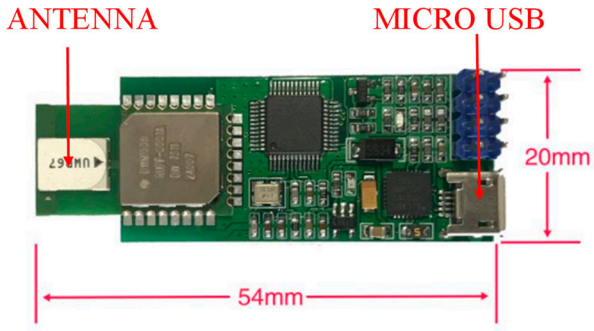

Figure 1. The D-DWM-PG 1.7 UWB module.

Table 1. Main technical specification of the D-DWM-PG 1.7 UWB module.

Indicator	Value
Range accuracy	±10 cm
Positioning accuracy	±30 cm
Rated voltage	DC 5 V
Rated current	250 mA
Communication rate	9600~256,000 bps
Single communication time	Minimum 0.2 ms–6.8 Mbps air speed
Single distance measurement time	Minimum 3 ms–6.8 Mbps air speed
Single positioning time	Minimum 20 ms–6.8 Mbps air speed
Communication distance	50 m
Communication frequency	3.5 GHz–6.5 GHz

Supposing there are four base stations and one tag, the observation equation can be expressed as

$$\begin{cases} (x-x_1)^2+(y-y_1)^2+(z-z_1)^2=R_1^2 \\ (x-x_2)^2+(y-y_2)^2+(z-z_2)^2=R_2^2 \\ (x-x_3)^2+(y-y_3)^2+(z-z_3)^2=R_3^2 \\ (x-x_4)^2+(y-y_4)^2+(z-z_4)^2=R_4^2 \end{cases} \quad (1)$$

where (x, y, z) is the coordinate of the tag, (x_i, y_i, z_i) is the coordinate of the ith base station, and R_i is the distance between the tag and the ith base station.

Therefore, the coordinate of the tag can be computed according to Equation (2),

$$\begin{bmatrix} x \\ y \\ z \end{bmatrix} = \frac{1}{2} N^{-1} B \tag{2}$$

where $N = \begin{bmatrix} 2(x_1 - x_2)\ 2(y_1 - y_2)\ 2(z_1 - z_2) \\ 2(x_1 - x_3)\ 2(y_1 - y_3)\ 2(z_1 - z_3) \\ 2(x_1 - x_4)\ 2(y_1 - y_4)\ 2(z_1 - z_4) \end{bmatrix}$,

$\mathrm{B} = \begin{bmatrix} R_2^2 - R_1^2 - x_2^2 + x_1^2 - y_2^2 + y_1^2 - z_2^2 + z_1^2 \\ R_3^2 - R_1^2 - x_3^2 + x_1^2 - y_3^2 + y_1^2 - z_3^2 + z_1^2 \\ R_4^2 - R_1^2 - x_4^2 + x_1^2 - y_4^2 + y_1^2 - z_4^2 + z_1^2 \end{bmatrix}$.

2.2. The Robotic Total Station

An RTS consists of precise angle and distance measuring mechanisms and tilt sensors, which can determine the three-dimensional coordinates of the target at the millimeter level. Its measurement principle can be expressed as

$$\begin{cases} x = x_S + S \times \cos\alpha \times \cos A \\ y = y_S + S \times \cos\alpha \times \sin A \\ z = z_S + S \times \sin\alpha + i - v \end{cases} \tag{3}$$

where (x, y, z) is the coordinate of the target, (x_S, y_S, z_S) is the coordinate of the RTS's station, S is the slope distance between the station and the target, α is the vertical angle, A is the azimuth of the line between the station and the target, and i and v represent the height of the instrument and target, respectively.

The MS60 multi-station RTS, a product of Leica Geosystems with its headquarters located in Heerbrugg, Switzerland, was utilized in our experimental setup. The main technical specifications are shown in Table 2. It can be seen that the accuracy of the MS60 angular and distance measurements is very high. When using the continuous tracking mode, the distance measurement frequency can reach up to 20 Hz, meeting the needs of dynamic positioning.

Table 2. Main technical indicators of the RTS Leica MS60.

Indicator	Value
Angular accuracy	0.5″
Distance accuracy and time	1 mm + 1.5 ppm (standard mode, 1.5 s) 3 mm + 1.5 ppm (continuous mode, 0.05 s)
Minimum working distance	1.5 m
Maximum range	GPR1prism: 10 km; GRZ4/GRZ122prism: 3 km; GRZ101prism: 1.5 km; non-prism: 2.4 km
Maximum allowed speed for locked prism	Tangential: 9 m/s (20 m), 45 m/s (100 m) Radial: 5 m/s

2.3. The Experimental System

The experimental system consists of three parts: an RTS subsystem, a UWB subsystem, and a PC. The connection relationship between them is shown in Figure 2. The control software, which runs on the PC, communicates with the RTS and UWB through WiFi and USB interfaces, respectively. The UWB tag and the 360° prism are bound together as the moving target and are mounted on the top of a surveying pole (see Figure 3). The vertical offset between the UWB antenna and the center of the prism is precisely determined by the RTS observation, and the horizontal offset is omitted since it is minimal. The z coordinate of the prism (retrieved through RTS) will be converted to the UWB antenna by adding the vertical offset.

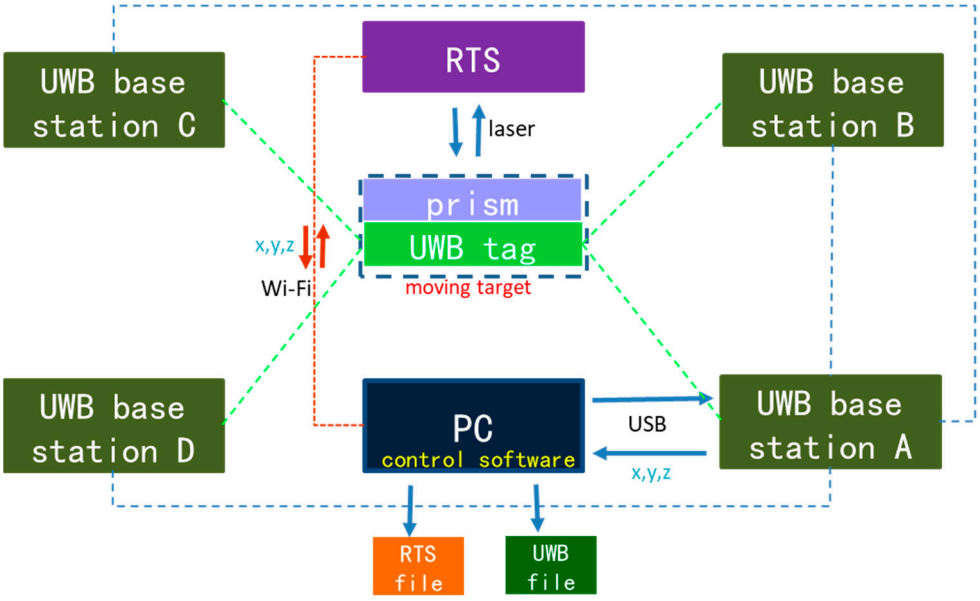

Figure 2. Schematic diagram of the hardware and software system.

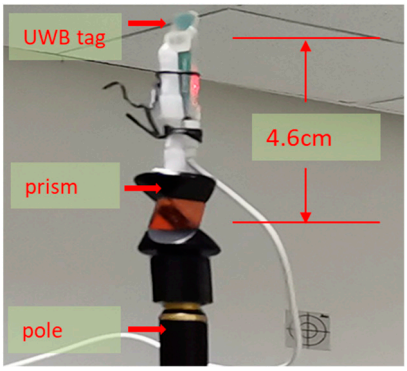

Figure 3. The structure diagram of the moving target, whose coordinates can be observed by the UWB and the RTS synchronously. The vertical offset between the UWB antenna and the center of the prism is 4.7 cm, which is used to convert the z coordinate observed by the RTS from the prism center to the UWB tag.

The control software can send orders to control the RTS and UWB, and receive their response messages. Once the RTS successfully locks the prism, and the UWB system starts to solve the tag's position, the control software will save their observations (containing time stamps) on the PC as two separate files. After completion of the data acquisition, the two files will be matched to compute the UWB's positioning errors.

2.4. Observation Matching

Due to the different sampling rates of RTS and UWB observations, the moments at which RTS and UWB record their coordinates are usually different. To obtain the benchmark value for the UWB's location at a moment T1, the RTS positioning coordinates at the two adjacent moments t1 and t2 are interpolated linearly to the moment T1 (see also Figure 4) as follows:

$$L(T1) = \frac{\triangle t1}{\triangle t} L(t2) + \frac{\triangle t2}{\triangle t} L(t1) \tag{4}$$

where L represents any component of the RTS coordinates (x, y, or z), the variable in the bracket denotes its moment, and $\triangle t$ is $t2 - t1$, $\triangle t1$ is $T1 - t1$, and $\triangle t2$ is $t2 - T1$.

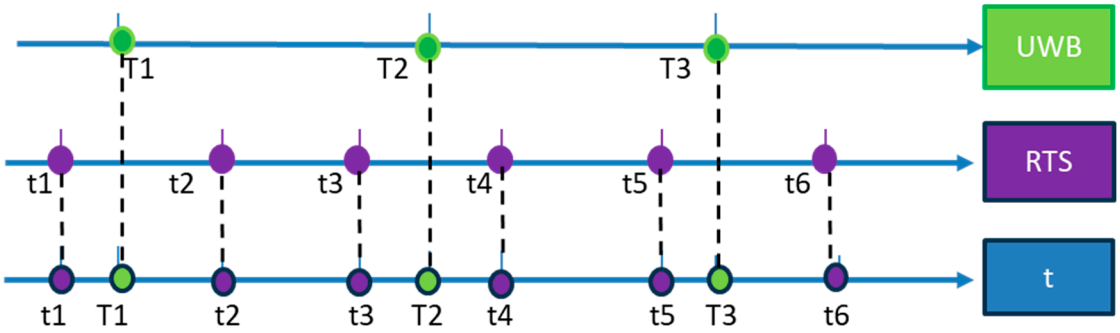

Figure 4. Principle of the observation matching.

To ensure the accuracy of the interpolation, both the time threshold for $\triangle t1$ and $\triangle t2$ and the displacement threshold for $L(t1)$-$L(t2)$ are set. Interpolation is only implemented when $|\triangle t1| < 0.5$ s and $|\triangle t2| < 0.5$ s and $|L(t1) - L(t2)| < 0.1$ m.

3. Design of The Experiment

3.1. The Experimental Steps

The experiment was conducted in a typical indoor environment laboratory, as shown in Figure 5. To simulate the NLOS condition, UWB stations A, C, and D were specially installed in obstructed positions. A was surrounded by several metal baffles, and C was mounted at the end of a narrow corridor. D was installed at the edge of the window near the ceiling, about 20 cm higher than the lower edge of the ceiling. Therefore, in the vast majority of the experiment locations, the UWB tag can only receive a clear LOS propagation condition from the UWB station B.

Figure 5. The panorama view of the experimental scene. A, B, C, and D each denote a distinct UWB base station.

The detailed experimental steps are listed below:

- The RTS was set up on a tripod with visibility to all four UWB base stations.
- The RTS's WLAN was connect to the PC's mobile hotspot so that the control software could communicate with the RTS.

- The UWB stations A, B, C, and D were mounted as shown in Figure 5, connecting the UWB station A interface to the PC through a USB cable to establish the data communication between the whole UWB system and the PC.
- The RTS measured the x, y, and z coordinates of each UWB station antenna, as shown in Table 3, recorded them using the control software, and then wrote them into the UWB system. In this way, the coordinates measured by the RTS and the UWB were unified into the same coordinate system.
- The moving target was mounted on the top of a surveying pole, including a prism and a UWB tag.
- The RTS was allowed to aim at the moving target roughly and before starting to lock the prism.
- The UWB system was allowed to start calculating the position of the tag.
- The control software was allowed to record the RTS and UWB observations as two separate files, and then, the surveying pole moved around the room.
- The experiment was terminated when enough observations were collected.
- Matching the RTS and UWB observation files, the UWB's positioning errors in the x, y, and z directions were calculated.
- A neural network was constructed to train the matched observation files. The structure diagram of the neural network is shown in Figure 6. The divisions of the dataset are shown in Figure 7.
- The accuracy of the network was evaluated by a verification dataset, which the trained network has not used.

Table 3. The 3D coordinates of the four UWB base stations.

UWB Base	x (m)	y (m)	z (m)
A	57.52	506.94	6.13
B	57.28	500.83	7.78
C	49.91	495.88	5.25
D	48.62	506.14	8.13

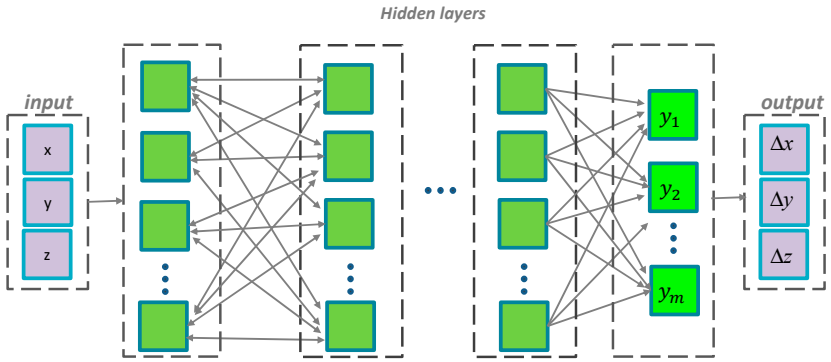

Figure 6. The structure diagram of the neural network.

3.2. Design of the Neural Network

The neural network gains its name from its brain-like structure, composed of the input, hidden, and output layers. In this study, we designed two kinds of neural networks, i.e., the combined and separate networks, depending on whether the three coordinate components x, y, and z use the same neural network. As can be seen in Figure 6, for the combined network, there are three outputs ($\triangle x$, $\triangle y$, $\triangle z$) in the output layer. While for the separate ones, each network has only one output (one of $\triangle x$, $\triangle y$, and $\triangle z$). The detailed parameters of each network's structure are listed in Table 4. The training function is the Bayesian Regularization, which can train the network by optimizing the Levenberg–Marquardt algorithm by updating the bias and weights. It minimizes a combination of squared errors and weights, and then determines the correct combination to produce a network that

generalizes well. The mean squared normalized error performance function was used as the performance function.

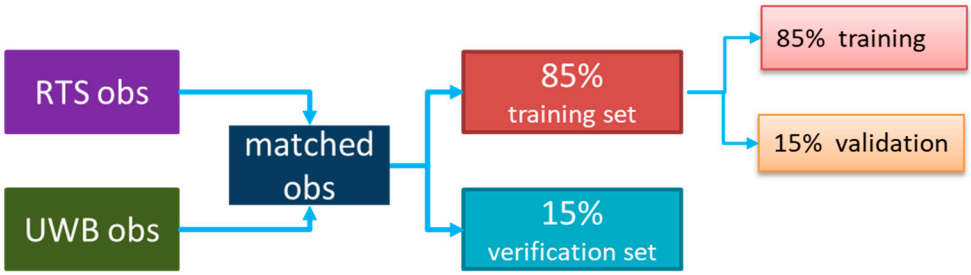

Figure 7. The divisions of the observation dataset. A total of 85% of the matched observations were used for training the neural network, and the remaining 15% were used to verify the external coincidence accuracy of the trained neural network.

Table 4. The structure of the neural network in this study.

Type of Network	Input	Structure of Hidden Layers	Output
Combined	x y z	$23 \times 9 \times 6 \times 3$	$\triangle x$ $\triangle y$ $\triangle z$
Separate	x	13×4	$\triangle x$
	y	13×4	$\triangle y$
	z	$22 \times 7 \times 5 \times 3$	$\triangle z$

$x\triangle x\triangle y\triangle z\triangle x\triangle y\triangle z$ The dataset is usually divided into three subsets when training the neural network. The first subset, i.e., the training set, is used to update the network by computing the gradient. The second subset is the validation set, which monitors errors during training. Typically, if the validation error decreases, as does the training set error. However, if the network overfits the data, the error on the validation set will rise. The weights and biases of the neural network are saved when the minimum of the validation set error appears. The third subset is the verification set, of which, the error is used to compare various models. A poor division of the dataset will lead to the error on the verification set reaching a minimum at a significantly different iteration number than the validation set error.

3.3. Traditional Methods

3.3.1. Polynomial Model

The polynomial model uses a polynomial formula to construct a surface that corresponds with the sample data using the following formulas:

$$f = \sum_{i=0}^{5} \sum_{j=0}^{5-i} p_{ij} x^i y^j \tag{5}$$

where p_{ij} is the model coefficient.

3.3.2. Locally Weighted Linear Regression

The locally weighted linear regression uses the weight of each sample to improve the algorithm's performance by using a parameter to control the change rate of weight to find the best model. The weights of each point are calculated by

$$w_i = \left(1 - \left|\frac{x - x_i}{d(x)}\right|^3\right)^3 \tag{6}$$

where x is the predictor value associated with the response value to be smoothed, x_i is the nearest neighbor of x as defined by the span, and d(x) is the distance along the abscissa from x to the most distant predictor value within the span.

3.4. Accuracy Indicators

Bias and the Root Mean Square Error (RMSE) are widely recognized as crucial metrics for assessing accuracy in the domains of positioning and navigation, including UWB [29–31]. Bias is a measure of the average error across all measurements, reflecting the systematic deviation from the true value. It reveals any consistent overestimation or underestimation by the system. On the other hand, the RMSE quantifies the average squared difference between the model's predictions and the true values. As a quadratic scoring rule, the RMSE offers an insightful measure of accuracy and precision. It accounts for the magnitude and direction of the errors, providing a robust assessment of the system's performance. Bias and the RMSE offer a holistic evaluation of a model's efficacy when used in tandem. They complement each other by highlighting systematic errors (bias) and the overall dispersion of errors (RMSE), thus giving a more complete picture of the model's performance and reliability. This dual approach enables researchers to refine their models and improve overall accuracy.

We calculated the bias and the Root Mean Square Error (RMSE) of the UWB positioning error according to the following formulas:

$$\begin{cases} \Delta_i = \mathrm{L}_i(UWB) - \mathrm{L}_i(RTS) \\ \mathrm{Bias} = \sum_{i=1}^{n} \Delta_i / n \\ \mathrm{RMSE} = \sqrt{\sum_{i=1}^{n} \Delta_i^2 / n} \end{cases} \tag{7}$$

where Δ is the positioning error, L represents the coordinate observation in the x, y, or z component, and n denotes the number of matched observations.

Two kinds of accuracy metrics are computed, including internal and external coincidence accuracy, which refers to the result from the training and verification sets, respectively. The internal coincidence accuracy mainly reflects the fitting effect, while the external coincidence accuracy can better measure the generalization ability of the neural network.

4. Results and Discussion

4.1. Result of the UWB Positioning Error

Figure 8 shows the trajectories of the matched UWB and RTS observations. The trajectory of UWB experienced the most severe drifts at the top left edge areas, where the NLOS error would be greater than elsewhere.

We computed the statistical result in Table 5. It is evident that the order of errors in the z component is much larger than that of the other two components, mainly due to the geometric distribution of the UWB base stations in the z component being worse. The bias of the UWB positioning errors in the x and y components are about 10 cm, while −52.5 cm in the z component. The RMSE values are 21.1 cm, 21.7 cm, and 89.2 cm in the x, y, and z components, respectively, which means that the UWB system's total three-dimensional positioning error reaches up to 94.2 cm, more than three times the nominal value in Table 1. Furthermore, the maximum error in the x and y components is nearly 50 cm for 95% of samples and ~1 m for 100%. In contrast, the 2D location accuracy of the DW1000 chip in the LOS condition reported by Barbara et al. is 25 cm for 95% and 32 cm for 100% [32]. It is evident that NLOS conditions have severely degraded the accuracy of UWB positioning.

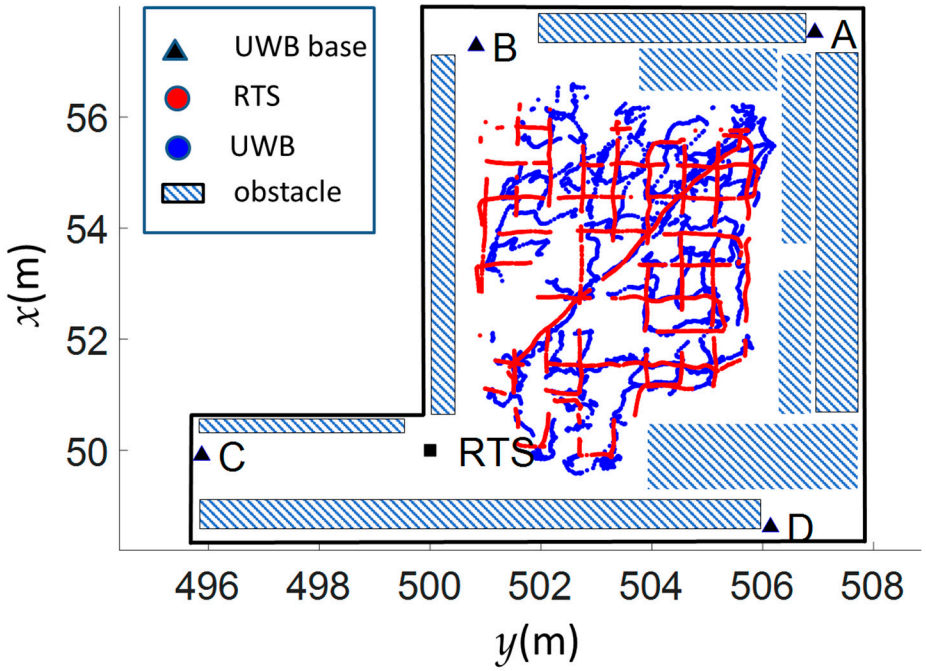

Figure 8. Trajectories of the matched UWB (blue) and RTS (red) observations. A, B, C, and D each denote a distinct UWB base station.

Table 5. Statistical results of the UWB positioning errors (cm).

	x	*y*	*z*
Bias	−10.9	−9.8	−52.5
RMSE	21.1	21.7	89.2
95% MAX	41.5	47.2	179.0
100% MAX	90.3	94.9	249.5

Figure 9 shows the arrow diagram of the UWB positioning error versus the reference value (RTS coordinate). Each arrow in a figure shows both the direction and value of a UWB positioning error. There is a common tendency among the three subgraphs that each component exhibits a significant nonlinear distribution with solid relevance to location. However, the features of the x, y, and z components are different.

For the z component, the distribution pattern of errors is much more complicated than that of the x and y components. In the top left corner of Figure 8, the errors in the three components are significantly larger than elsewhere, mainly because the LOS signal between this area and the UWB station C was entirely blocked by the corridor wall, which led to a significant NLOS effect. Furthermore, the UWB base C was installed relatively lower compared with the other three base stations (less than 30 cm above the ground). Such geometric distribution of base stations plays a vital role in the UWB positioning accuracy on the z component.

4.2. Results of the Traditional Models and Neural Networks

As can be seen from Table 6, compared with the raw positioning error, the accuracy of the polynomial model and the locally weighted linear regression are very close to each other, of which, the RMSE reductions for the *x/y/z* components are ~50%. The combined network performs better than the two traditional models, of which, the external RMSE of errors is reduced by 55%, 52%, and 76% for the x, y, and z components, respectively. The separate networks perform best among all methods, by which the external RMSE is reduced by 66%, 71%, and 80% for the x, y, and z components, respectively. These results indicate that the neural network can fit the UWB positioning errors well. Furthermore,

it would be better to construct a particular network for each component since their error distribution patterns are different.

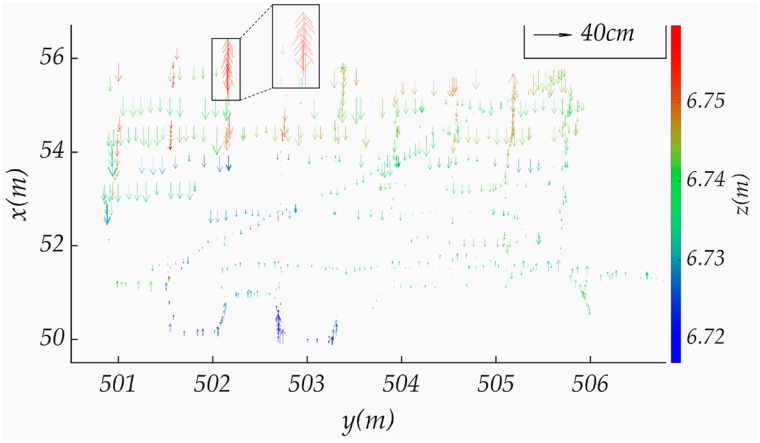

(**a**)

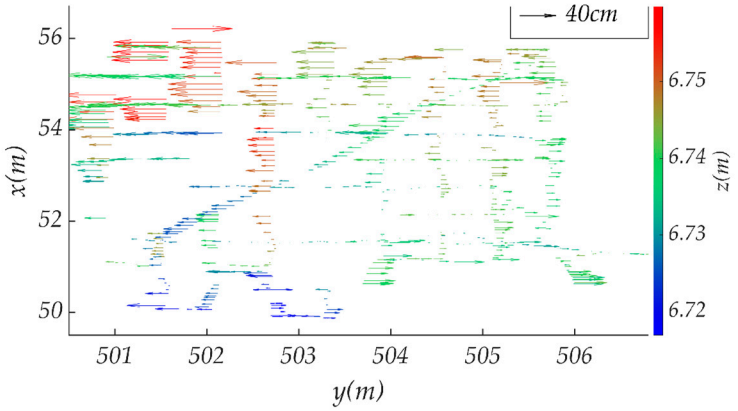

(**b**)

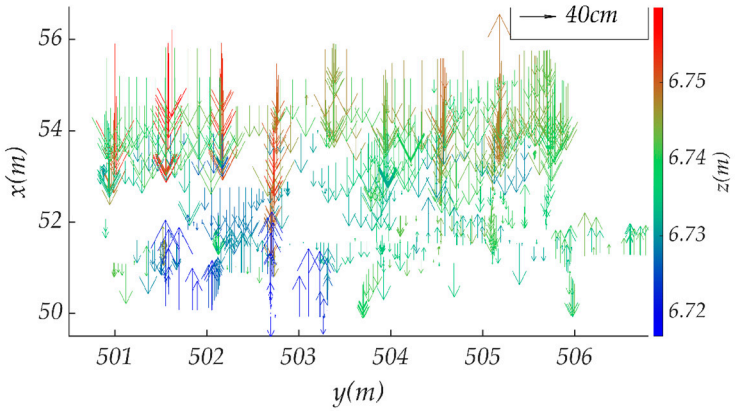

(**c**)

Figure 9. The arrow diagram of UWB positioning errors on three axes. The color of an arrow or a UWB station indicates its z value. The arrow is only drawn for every ten errors to avoid mutual obstruction. (**a**) UWB positioning error in the x component; (**b**) UWB positioning error in the y component; (**c**) UWB positioning error in the z component.

Table 6. Statistical results of the traditional methods and the neural networks.

Method	Statistic	Internal Accuracy			External Accuracy		
		x	*y*	*z*	*x*	*y*	*z*
Polynomial model	Bias (cm)	0.1	0.2	0.0	0.0	0.0	−1.8
	RMSE (cm)	10.7	9.9	41.9	11.0	10.5	41.9
	RMSE reduction	47%	54%	53%	47%	51%	53%
Locally weighted linear regression	Bias (cm)	0.0	0.1	0.2	0.0	0.5	0.4
	RMSE (cm)	11.0	10.1	41.3	11.1	10.6	42.8
	RMSE reduction	47%	53%	54%	47%	51%	52%
Combined neural network	Bias (cm)	0.0	0.0	0.0	−0.4	1.0	−1.1
	RMSE (cm)	9.5	9.7	16.4	9.5	10.4	21.4
	RMSE reduction	55%	55%	82%	55%	52%	76%
Separate neural network	Bias (cm)	0.0	0.0	0.0	0.3	−0.6	0.2
	RMSE (cm)	5.5	5.9	15.3	7.2	6.2	18.2
	RMSE reduction	74%	73%	83%	66%	71%	80%

Figure 10 shows the residuals in the combined and separate neural networks' *x*, *y*, and *z* components. It can be noted that neural networks significantly reduce the position residuals. The histogram of UWB positioning errors for the raw observation and the trained neural network is shown in Figure 11. Compared with the former, the later errors present much more obvious accidental error characteristics, indicating good fitting performance.

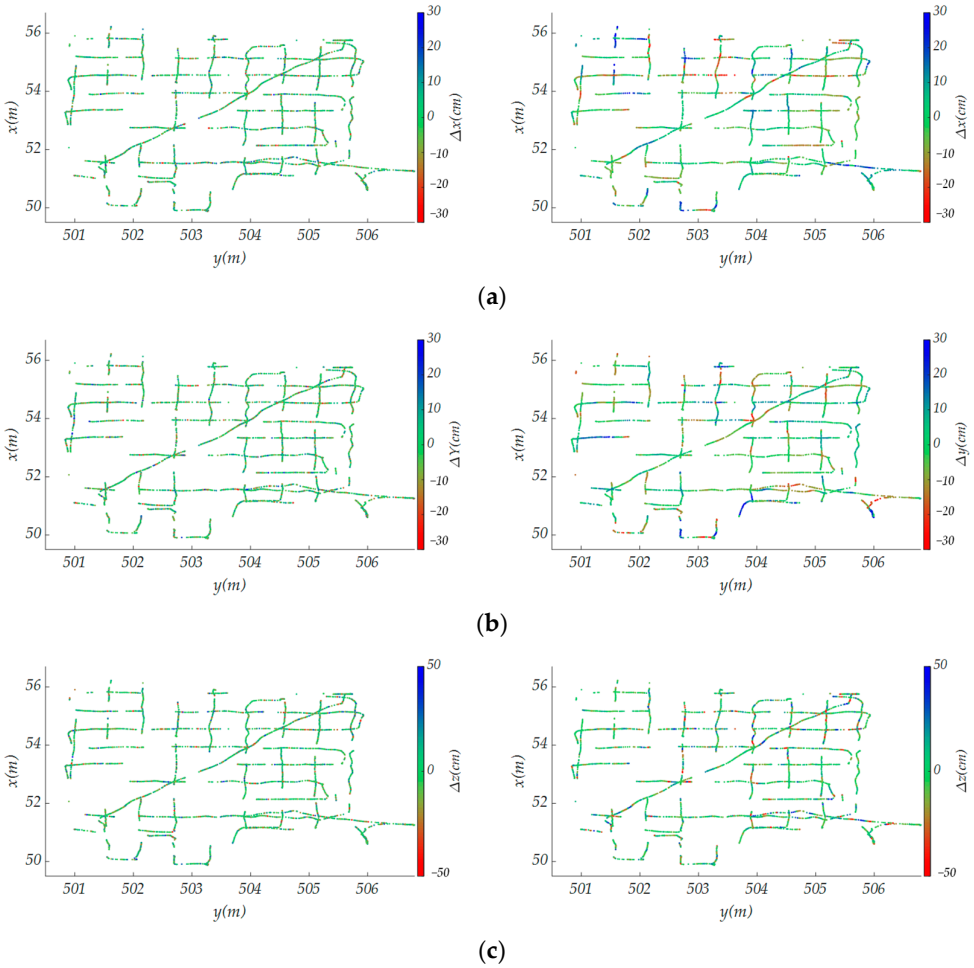

Figure 10. The UWB positioning error of the combined (left) and separate (right) networks. (**a**) Residuals in the *x*-component; (**b**) residuals in the *y*-component; (**c**) residuals in the *z*-component.

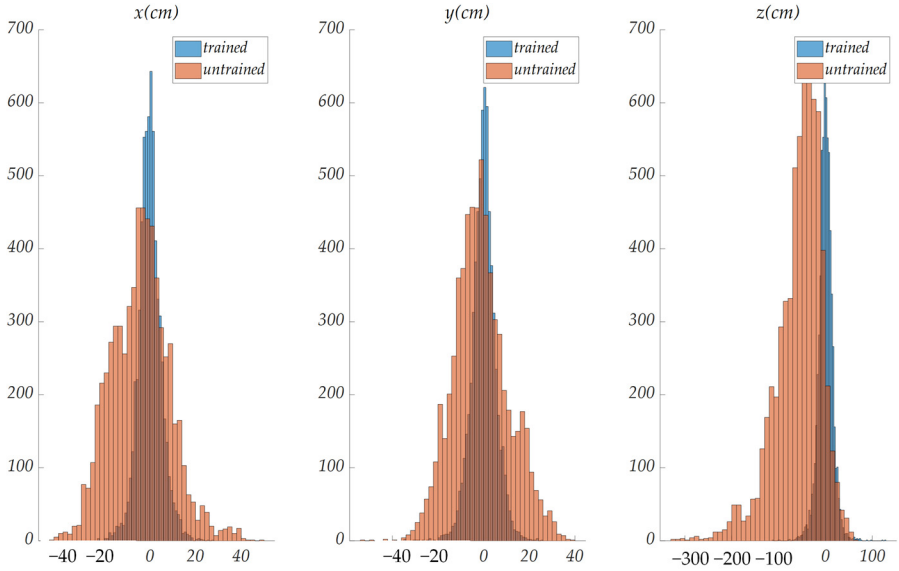

Figure 11. Histogram for raw (untrained) and separate (trained) networks derived from UWB positioning errors.

5. Conclusions

This study aims to improve the accuracy of UWB indoor positioning with significant NLOS conditions. We developed an experimental system, comprising a Leica MS60 high-precision RTS, four D-DWM-PG1.7 UWB base stations, and a moving target. The moving target is equipped with a coaxial reflective prism and a UWB tag. Based on the synchronous coordinates obtained by the RTS and the UWB system, the benchmark values of the UWB tag's positioning error are computed, of which, RMSE values are found to be 21.1 cm, 21.7 cm, and 89.2 cm in the x, y, and z components, respectively. NLOS conditions have severely degraded the UWB positioning accuracy, reducing it to less than one-third of the manufacturer's stated nominal value. Furthermore, distinct error distribution patterns have been observed across the three coordinate components.

Two kinds of multilayer neural networks were designed and compared, i.e., a combined network and three separate networks. Both neural networks take three-dimensional coordinates as input values. However, the former outputs three coordinate components at a time, and the latter only fits one of the three coordinate components for each model. The results of employing benchmark errors as the training and verification datasets for neural networks showed that both networks had better performances than the traditional models. Specifically, they achieved an average reduction in RMSE of positioning errors by 61% and 72%, respectively. The separate networks perform better than the combined network since they are able to handle the error distribution pattern more precisely in each coordinate component. This customized strategy facilitates more accurate optimization and management of errors, leading to better modelling effects compared to a combined network configuration.

Author Contributions: Conceptualization, Y.W. and D.Z.; methodology, D.Z.; software, D.Z. and M.L.; validation, Z.L. and Y.Z.; formal analysis, Z.L. and M.L.; investigation, M.L. and Y.Z.; resources, Y.W. and T.F.; data curation, Y.Z. and M.L.; writing—original draft preparation, Y.W. and T.F.; writing—review and editing, D.Z.; visualization, M.L. and Y.W.; supervision, Z.L.; project administration, D.Z.; funding acquisition, D.Z. and Z.L. All authors have read and agreed to the published version of the manuscript.

Funding: This research was supported by the China Postdoctoral Science Foundation (2021MD703896), Yunnan Fundamental Research Projects (grant NO. 202301AU070101), the Fundamental Research Funds for the Central Universities (2042023kf0002), and the Hubei Provincial Natural Science Foundation of China (2022CFB090).

Data Availability Statement: Data are contained within the article.

Conflicts of Interest: Author Yifan Wang was employed by the company Joint Laboratory of Power Remote Sensing Technology, Electric Power Research Institute, Yunnan Power Grid Co., Ltd. The remaining authors declare that the research was conducted in the absence of any commercial or financial relationships that could be construed as a potential conflict of interest.

References

1. Zhao, Y.Z.; Zou, J.G.; Guo, J.M.; Huang, G.G.; Cai, L.X. A Novel Ultra-Wideband Double Difference Indoor Positioning Method with Additional Baseline Constraint. *ISPRS Int. J. Geo-Inf.* **2021**, *10*, 634. [CrossRef]
2. Li, X.; Li, H.; Huang, G.; Zhang, Q.; Meng, S. Non-holonomic constraint (NHC)-assisted GNSS/SINS positioning using a vehicle motion state classification (VMSC)-based convolution neural network. *GPS Solut.* **2023**, *27*, 144. [CrossRef]
3. Grasso, P.; Innocente, M.S.; Tai, J.J.; Haas, O.; Dizqah, A.M. Analysis and Accuracy Improvement of UWB-TDoA-Based Indoor Positioning System. *Sensors* **2022**, *22*, 9136. [CrossRef]
4. Bastida Castillo, A.; Gómez Carmona, C.D.; De la cruz sánchez, E.; Pino Ortega, J. Accuracy, intra- and inter-unit reliability, and comparison between GPS and UWB-based position-tracking systems used for time–motion analyses in soccer. *Eur. J. Sport Sci.* **2018**, *18*, 450–457. [CrossRef] [PubMed]
5. Kim Geok, T.; Zar Aung, K.; Sandar Aung, M.; Thu Soe, M.; Abdaziz, A.; Pao Liew, C.; Hossain, F.; Tso, C.P.; Yong, W.H. Review of Indoor Positioning: Radio Wave Technology. *Appl. Sci.* **2021**, *11*, 279. [CrossRef]
6. Ridolfi, M.; Vandermeeren, S.; Defraye, J.; Steendam, H.; Gerlo, J.; De Clercq, D.; Hoebeke, J.; De Poorter, E. Experimental Evaluation of UWB Indoor Positioning for Sport Postures. *Sensors* **2018**, *18*, 168. [CrossRef]
7. Cheng, S.; Wang, X.; Zhang, H. Application of firefly algorithm to UWB indoor positioning. In Proceedings of the 2021 IEEE 11th Annual Computing and Communication Workshop and Conference (CCWC), Las Vegas, NV, USA, 27–30 January 2021; pp. 88–93.
8. Park, J.; Cho, Y.K.; Martinez, D. A BIM and UWB integrated mobile robot navigation system for indoor position tracking applications. *J. Constr. Eng. Proj. Manag.* **2016**, *6*, 30–39. [CrossRef]
9. Wang, Y.; Chen, X.; Shi, L.; Cheng, Y.; Wang, H. A Trust Assessment-Based Distributed Localization Algorithm for Sensor Networks Under Deception Attacks. *IEEE/CAA J. Autom. Sin.* **2022**, *9*, 4. [CrossRef]
10. Barral, V.; Escudero, C.J.; García-Naya, J.A.; Maneiro-Catoira, R. NLOS Identification and Mitigation Using Low-Cost UWB Devices. *Sensors* **2019**, *19*, 3464. [CrossRef]
11. Zafari, F.; Gkelias, A.; Leung, K.K. A survey of indoor localization systems and technologies. *IEEE Commun. Surv. Tutor.* **2019**, *21*, 2568–2599. [CrossRef]
12. Koiloth, S.J.; Achanta, D.S.; Koppireddi, P.R. ML-based LOS/NLOS/multipath signal classifiers for GNSS in simulated multipath environment. *Aerospace Systems* **2023**, *7*, 237–250. [CrossRef]
13. Cimdins, M.; Schmidt, S.O.; Hellbrück, H. MAMPI-UWB—Multipath-assisted device-free localization with magnitude and phase information with UWB transceivers. *Sensors* **2020**, *20*, 7090. [CrossRef]
14. Deng, W.; Li, J.; Tang, Y.; Zhang, X. Low-Complexity Joint Angle of Arrival and Time of Arrival Estimation of Multipath Signal in UWB System. *Sensors* **2023**, *23*, 6363. [CrossRef] [PubMed]
15. Zwirello, L.; Schipper, T.; Harter, M.; Zwick, T. UWB Localization System for Indoor Applications: Concept, Realization and Analysis. *J. Electr. Comput. Eng.* **2012**, *2012*, 849638. [CrossRef]
16. Feng, D.; Wang, C.; He, C.; Zhuang, Y.; Xia, X.-G. Kalman-filter-based integration of IMU and UWB for high-accuracy indoor positioning and navigation. *IEEE Internet Things J.* **2020**, *7*, 3133–3146. [CrossRef]
17. Zhouzheng, G.; Yan, L.; Lin, C. An ultra-wideband based credible indoor positioning method by considering geometry-distribution and NLOS signal. *Navig. Position. Timing* **2023**, *10*, 16–24.
18. Songcan, Y.; Yongxin, L.; Gen, L. Twice Correction Indoor Positioning Algorithm Using Ultra-Wideband Technology. In Proceedings of the 2019 Chinese Automation Congress (CAC), Hangzhou, China, 22–24 November 2019; pp. 3748–3753.
19. Zhang, H.; Zhang, Z.; Zhao, R.; Lu, J.; Wang, Y.; Jia, P. Review on UWB-based and multi-sensor fusion positioning algorithms in indoor environment. In Proceedings of the 2021 IEEE 5th Advanced Information Technology, Electronic and Automation Control Conference (IAEAC), Chongqing, China, 12–14 March 2021; pp. 1594–1598.
20. Zhu, Y.; Luo, X.; Guan, S.; Wang, Z. Indoor positioning method based on WiFi/Bluetooth and PDR fusion positioning. In Proceedings of the 2021 13th International Conference on Advanced Computational Intelligence (ICACI), Wanzhou, China, 14–16 May 2021; pp. 233–238.
21. Guosheng, W.; Shuqi, Q.; Qiang, L.; Heng, W.; Huican, L.; Bing, L. UWB and IMU system fusion for indoor navigation. In Proceedings of the 2018 37th Chinese Control Conference (CCC), Wuhan, China, 25–27 July 2018; pp. 4946–4950.
22. Jiang, C.; Shen, J.; Chen, S.; Chen, Y.; Liu, D.; Bo, Y. UWB NLOS/LOS classification using deep learning method. *IEEE Commun. Lett.* **2020**, *24*, 2226–2230. [CrossRef]
23. Paszek, K.; Grzechca, D.; Becker, A. Design of the UWB positioning system simulator for LOS/NLOS environments. *Sensors* **2021**, *21*, 4757. [CrossRef]

24. Napoletano, P.; Piccoli, F.; Schettini, R. Anomaly Detection in Nanofibrous Materials by CNN-Based Self-Similarity. *Sensors* **2018**, *18*, 209. [CrossRef]
25. Li, B.; Zhao, K.; Sandoval, E.B. A UWB-Based Indoor Positioning System Employing Neural Networks. *J. Geovisualization Spat. Anal.* **2020**, *4*, 18. [CrossRef]
26. Nosrati, L.; Fazel, M.S.; Ghavami, M. Improving indoor localization using mobile UWB sensor and deep neural networks. *IEEE Access* **2022**, *10*, 20420–20431. [CrossRef]
27. Zhang, D.; Fang, T.; Ai, J.; Wang, Y.; Zhou, L.; Guo, J.; Mei, W.; Zhao, Y. UAV/RTS system based on MMCPF theory for fast and precise determination of position and orientation. *Measurement* **2022**, *187*, 110342. [CrossRef]
28. Vaidis, M.; Dubois, W.; Gu'enette, A.; Laconte, J.; Kubelka, V.; Pomerleau, F. Extrinsic calibration for highly accurate trajectories reconstruction. In Proceedings of the 2023 IEEE International Conference on Robotics and Automation (ICRA), London, UK, 29 May–2 June 2023.
29. Arsuaga, M.; Ochoa-De-Eribe-Landaberea, A.; Zamora-Cadenas, L.; Arrizabalaga, S.; Velez, I. Novel Classification Method to Predict the Accuracy of UWB Ranging Estimates. *IEEE Access* **2024**, *12*, 33659–33670. [CrossRef]
30. Tchoffo Talom, F.; Denis, B.; Keignart, J.; Daniele, N.; Bouix, D. UWB positioning experiment in a typical snowy environment. In Proceedings of the 4th Workshop on Positioning, Navigation and Communication 2007 (WPNC 07), Lepniz Univ Hannover, Hannover, Germany, 22 March 2007; pp. 65–70.
31. Yang, G.; Zhao, L.; Dai, Y.; Xu, Y. A KI-T-TOA UWB Indoor Positioning Method for Complex Environment. In Proceedings of the Chinese Automation Congress (CAC), Jinan, China, 20–22 October 2017; pp. 3010–3014.
32. Morawska, B.; Lipiński, P.; Lichy, K.; Koch, P.; Leplawy, M. Static and Dynamic Comparison of Pozyx and DecaWave UWB Indoor Localization Systems with Possible Improvements. In *International Conference on Computational Science*; Springer: Cham, Switzerland, 2021; pp. 582–594.